Microchemical Journal 226 (2026) 118281

Contents lists available at ScienceDirect

Microchemical Journal

journal homepage: www.elsevier.com/locate/microc

Enhanced photoelectrochemical immunosensing of carcinoembryonic antigen via MoS_2 heterostructure-induced charge separation

Syeda Ammara Shabbir [a,d,*], Amna Shahzad [a], Raheel Shamir Farhat [a], Muhammad Haris [b,c], Maryam Tahir [a], Safia Anjum [e], Hamid Latif [a], Carlos Ponce de Leon [d], Rezwan Ullah [f], Tomas Tamulevičius [b,c], Sigitas Tamulevičius [b,c]

[a] Department of Physics, Forman Christian College (A Chartered University), Lahore, Pakistan
[b] Institute of Materials Science, Kaunas University of Technology, K. Baršausko g. 59, LT51423 Kaunas, Lithuania
[c] Department of Physics, Kaunas University of Technology, Lithuania Studentų St. 50, LT51368, Kaunas, Lithuania
[d] Department of Mechanical Engineering, Faculty of Engineering and Physical Sciences, University of Southampton, Highfield Campus, Southampton SO17 1BJ, UK
[e] Department of Physics, Lahore College for Women University, Lahore, Pakistan
[f] Department of Aeronautical Engineering, Faculty of Mechanical Engineering and Design, Kaunas University of Technology, Lithuania

ARTICLE INFO

Keywords:
Photoelectrochemical Immunosensor
MoS_2 heterostructure
Carcinoembryonic antigen
Z-scheme charge transfer
Cancer biomarker detection

ABSTRACT

Photoelectrochemical (PEC) biosensors have great potential in the detection of biomarkers in an ultra-sensitive manner. However, many of the PEC biosensors have poor carrier recombination and charge separation. In this project, a PEC Immunosensor based on a MoS_2 heterostructure has been synthesized for detecting carcinoembryonic antigens (CEAs) through the formation of bismuth oxyiodide (BiOI) composite with reduced graphene oxide (rGO). The fabricated rGO/MoS_2/BiOI obtained a greater visible light absorption capacity and an improved band gap of about 1.19 eV facilitating optimum photo-absorption (excitation) under visible light. Upon photoelectrochemical testing, the rGO/MoS_2/BiOI ternary electrode exhibited a photocurrent density of about 25.6 mA which dropped to about 4.0 mA due to the formation of antigen-antibody complexes signifying great charge transfer in the interface. Mott Schottky analysis confirmed the presence of a p-p heterojunction and *Z*-scheme for the charge transfer system which effectively lowered the recombination rate of the electron-hole pairs. The developed rGO/MoS_2/BiOI PEC immunosensor exhibited excellent stability and selectivity, delivering consistent photocurrent responses under repeated light on/off cycles with minimal interference from other biomolecules. It showed a linear response toward CEA over a wide concentration range (0.01–10 μg/mL) with a low detection limit of 0.01 μg/mL, demonstrating its strong potential for sensitive and reliable biomarker detection. This research demonstrated the promising properties of MoS_2 based heterostructure PEC Immunosensor for early cancer diagnostics.

1. Introduction

Effective diagnosis, prognosis, and therapeutic monitoring require early and precise detection of cancer biomarkers. Carcinoembryonic antigen (CEA) is a significant tumor marker that is clinically used for screening and monitoring of colorectal, lung, breast, and pancreatic cancer. Screening for CEA as a cancer biomarker is complicated since, early in disease progression, CEA is usually present in very low concentrations. Moreover, detecting CEA in complex biological matrices is very challenging [1]. Traditional analytical methods, such as enzyme-linked immunosorbent assays, fluorescence-based approaches, and chemiluminescence assays require intensive manual work, expensive analytical equipment, and long assay durations. Furthermore, these approaches do not provide enough sensitivity at trace concentrations. These challenges in CEA biomarker detection have led to the design of unconventional, more sensitive, less obstructed, and faster analytical methods [2]. In this regard, photoelectrochemical (PEC) Immunosensor are considered to be one of the most promising platforms. Having the light source (excitation) separated from the signal detection (photocurrent) provides the advantage of reducing background signals, resulting in higher signal to noise ratios [3]. In PEC systems, the light irradiation of a photoactive electrode creates electron-hole pairs and the

---

* Corresponding author at: Department of Physics, Forman Christian College (A Chartered University), Lahore, Pakistan.
E-mail address: ammaraanwar@fccollege.edu.pk (S.A. Shabbir).

https://doi.org/10.1016/j.microc.2026.118281
Received 27 March 2026; Received in revised form 22 April 2026; Accepted 3 May 2026

resulting photocurrent is responsive to changes at the electrode/electrolyte interface [4]. A simple schematic representation of this PEC sensing is shown in Fig. 1, where the charge carriers that are generated from the interface are signal carriers. Therefore, PEC systems are applicable to bio sensing, as molecular recognition events are transduced to measurable signals. In this case, the binding of specific antibodies to antigens at the electrode surface changes the charge transfer at the interface [5].

Early investigations into PEC immunosensing demonstrated that sensor performance is critically governed by the nature, dimensionality, and interfacial architecture of the photoactive materials. [6] reported an ultrasensitive PEC Immunosensor for CEA based on two-dimensional TiO_2 Nano sheets coupled with carboxylated g-C_3N_4, showing that 2D nanostructures produce significantly higher photoelectrochemical responses than conventional nanoparticles due to improved charge separation and interfacial contact. Their results confirmed that photocurrent attenuation caused by antibody–antigen binding could be directly correlated with CEA concentration, validating the PEC approach for tumor marker detection.

The PEC research further developed heterostructure engineering to address the intrinsic rapid recombination of charge carriers and light-harvesting efficiency limitations of the single-component photoactive materials. Considerable work has already been published on the design and fabrication of PEC Immunosensor for example, fabricated a sandwich-type PEC Immunosensor using a 3D graphene oxide/MoS_2 composite as the photoactive layer, where the synergistic charge transport pathways enabled the pictogram-level detection of CEA [7]. Advanced Photo electrochemical immunosensor [8] indicated that in p–n heterojunctions like NiS@NiO/TiO_2, the photocurrent output was further enhanced by reduced recombination of electron–hole pairs and an extension of the absorption to the visible range. This study also made a split-type PEC biosensor using Bi_2S_3@BiOI heterostructure with in situ Ag_2S, where the optimized band alignment with multistage signal amplification enabled ultralow detection limits for CEA. Together, these research works confirmed the established heterostructure design as one of the fundamental tenets for the construction of high-performance PEC Immunosensor. Therefore, with regards to Bi-based semiconductors, BiOI has received a lot of focus. BiOI is a p-type semiconductor with a band gap of about 1.8 eV. The layered crystalline structure also allows for significant absorption in the visible spectrum. The rapid recombination of photogenerated charge carriers that is within that narrow band gap, however, limits the efficiency of PECs [9]. A study constructed BiOI/BiOCl heterojunctions for PEC immunosensing and achieved femtogram-level sensitivity for CEA under zero-bias conditions, noting interfacial charge transfer and internal electric fields responsiveness and stabilizing photocurrent responses [10]. Simultaneously, PEC architectures have been further advanced through the use of carbon-based materials. Among these, reduced graphene oxide (rGO) is often the preferred and most cost-effective option given its superior electrical conductivity, high surface area, and good electron-transport pathways. It is known that rGO is weakly photoactive, but combined with semiconductors, it promotes charge transfer, inhibits charge recombination, and possesses a significant photo inactive surface sufficient for the stable immobilization of antibodies. Therefore, the incorporation of rGO in PEC Immunosensor for the purpose of increasing sensitivity, stability, and selectivity is well justified [11].

A growing number of studies focused on PEC systems still tend to rely on semiconducting oxides and signal amplification techniques which increase the complexity of the fabrication and are detrimental to practical scalability [12]. As a result, there has been a growing interest in two-dimensional transition metal dichalcogenides (TMDs) which are considered potential next-generation PEC materials. TMD mono layers are typically designated as MX_2, where M is the transition metal and X the chalcogen. These are atomically thin semiconductors which possess tunable band gaps, high carrier mobilities, and strong light-matter interactions [13]. TMDs are a promising class of materials for PEC applications, particularly molybdenum disulfide (MoS_2) [14]. MoS_2 band gaps are tunable (1.9 eV for mono layers and 1.2 eV for bulk) enabling absorption of a significant amount of energy in the visible light range. Furthermore, the high specific surface area and the abundant active sites of the S–Mo–S sandwich structure, which is the representative structure of MoS_2, is advantageous for the immobilization of biomolecules, which is beneficial for PEC immunosensing. That said, pure MoS_2 does suffer from rapid recombination of the photo generated charge carriers and low photocurrent which limits its effectiveness [15]. Recent studies have shown that MoS_2-centered heterostructure can effectively mitigate these issues. When MoS_2 is combined with BiOI, a visible-light-active semiconductor, and rGO, a conductive material, a synergistic effect occurs where the system increases the light absorption, directional charge separation, and interfacial electron transfer. In such systems, MoS_2 is a charge transport mediator and provides a biocompatible surface for antibody binding, while BiOI provides the primary light absorption and rGO is the conduit of the charge transfer pathway [3,4,13,16]. In PEC immunosensing, the signal transduction is based on immunorecognition that alters charge transfer at the electrode interface. Antibody capture of Carcinoembryonic Antigen (CEA) on the MoS_2-based heterostructure,

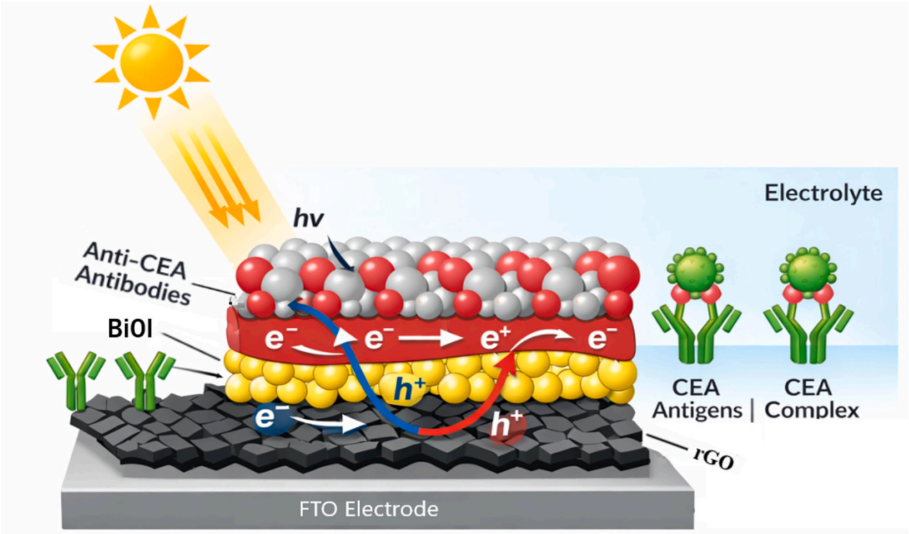

Fig. 1. Schematic representation of this PEC sensing.

forms an insulating layer of immunocomplex that increases the interfacial resistance of the electrode and impedes charge transfer. Thus, with increasing CEA concentration, the photocurrent diminishes proportionally, resulting in a signal-off PEC response for the quantification of the target [16].

While BiOI, MoS_2, and rGO have each shown great PEC characteristics, there is still not enough research on the integrating BiOI, MoS_2, and rGO into a MoS_2 centered heterostructure with a photo electrochemical immunosensing mechanism. More various roles of MoS_2 in controlling the absorption of light, charge separation, and the immobilization and modification of the antibodies within the PEC systems are brought into very little under considerations. To address some of these issues, this study developed a novel BiOI/MoS_2/rGO-based photo electrochemical Immunosensor, and focused on the ultrasensitive detection of carcinoembryonic antigen. It tends to utilize the synergistic properties of the heterostructure to improve the photocurrent response, reduce the recombination, and facilitate the detection of early-stage cancer biomarkers.

2. Methodology

2.1. Fabrication of photoactive materials

The photoactive materials used in this study were synthesized using solvothermal and hydrothermal routes, selected for their ability to produce well-crystallized, morphologically controlled nanostructures with reproducible properties. All chemicals used were of analytical grade and were employed without further purification. Deionized water was used throughout the experimental procedures.

BiOI was synthesized via a solvothermal method using bismuth(III) nitrate pentahydrate [$Bi(NO_3)_3{\cdot}5H_2O$] and potassium iodide (KI) as precursor materials, with ethylene glycol serving as the reaction medium (Fig. 2). Initially, 1.46 g of $Bi(NO_3)_3.5H_2O$ and 0.5 g of KI were each separately, and thoroughly, mixed with 40 mL ethylene glycol. Upon full dissolution of KI, the solution was added to the stirring $Bi(NO_3)_3.5H_2O$ solution dropwise. After stirring for an hour, the mixture was transferred into a one hundred milliliter Teflon lined autoclave which was heated to 160 °C for twenty-four hours. Subsequently, the Teflon-lined autoclave was allowed to cool naturally to room temperature, during which time 200 mL deionized water was added gradually. The resulting mixture underwent centrifugation at 8000 rpm for five minutes yielding yellow BiOI powder precipitate which was dried at 80 °C for six hours [17].

rGO based composite of MoS_2 nanosheets were prepared by a one-step solvo thermal route (Fig. 3). To begin, sodium molybdate dihydrate (0.2 g $Na_2MoO_4{\cdot}2H_2O$), (50 mg $NaH_2PO_2.H_2O$) and thiourea (0.26 g) were dissolved in 5 mL of ethylene glycol; after stirring for 20 min, and 0.013 g of graphene oxide was added. The resulting solution was sonicated at room temperature for 2 h, then transferred to a custom 316 stainless-steel high-pressure cell fitted with Swagelok components rated to 400C. This cell, serving as an 8-mL autoclave, was placed in a thermostatic oven held at 350C for a 16-h isothermal reaction. After the designated time, the autoclave cooled to room temperature under natural convection. The black precipitate was collected by centrifugation and washed several times—three cycles each with distilled water followed by absolute ethanol—without drying in between to avoid particle aggregation and to make subsequent solvent removal easier after settling. Following these steps, the final product obtained was composed black residues which primarily contained rGO/MoS_2, which underwent drying at a steady temperature of 60 °C during twelve-hour duration in an oven designed for thermostatic conditions [18].

2.2. Fabrication of photo electrochemical immunosensor electrodes

Fluorine-doped tin oxide (FTO) glass substrates (1 cm × 1 cm) were employed as the conductive base for the electrodes. The substrate FTO glass was cleaned and prepared for conductive coating using a 3 step ultrasonic cleaning process: 1) the slides were sonicated in acetone for 30 min (to remove organic contaminants), 2) the slides were sonicated in ethanol for 30 min (to remove ethanol soluble contaminates), and 3) the slides were sonicated in deionized water (to remove contaminants from the previous two solvents). The FTO glass slides were then dried in a nitrogen stream. In order to compare electrodes with different materials, the following combinations were prepared: BiOI, MoS_2, rGO/BiOI, rGO/MoS_2, rGO/BiOI/MoS_2, and the hybrid materials BiOI/MoS_2. For each of the combinations, 10 μL of the respective solution was dispensed on clean FTO glass slides and allowed to air-dry to form a thin and uniform coating. The slides were placed in a furnace and sintered for 30 min at 450 °C and then allowed to cool to room temperature to minimize the chances of cracking or delaminating the films. In the end, in order to functionalize the electrodes for immunosensing, 10 μL of the respective antigen was spotted on each modified electrode surface. The electrodes were stored at 4 °C for 1 h to confirm proper binding between the photoactive material surface antigens and the photoactive material. This step assists in creating an antigen layer that interacts specifically with the biomarker CEA. After the antigen was immobilized, the active sites on the electrode surface were so that no unreacted sites would be able to react make non-specific interactions. To each electrode, 12 μL of Bovine Serum Albumin (BSA) Solution was added. BSA, as a blocking agent, form bio-inert layer, which ensures that the PEC signals will only be due

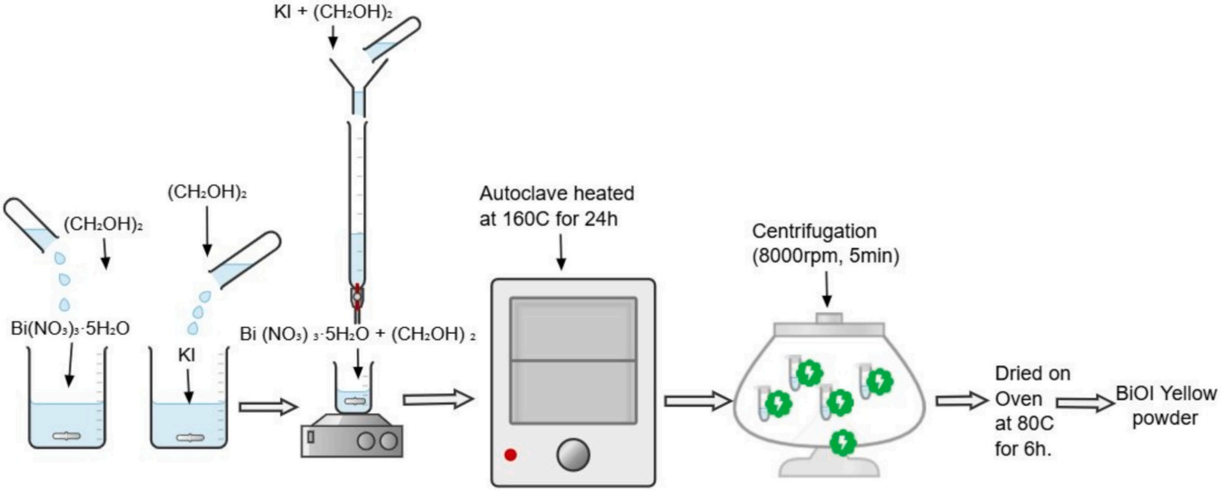

Fig. 2. Synthesis of BiOI nanoparticles.

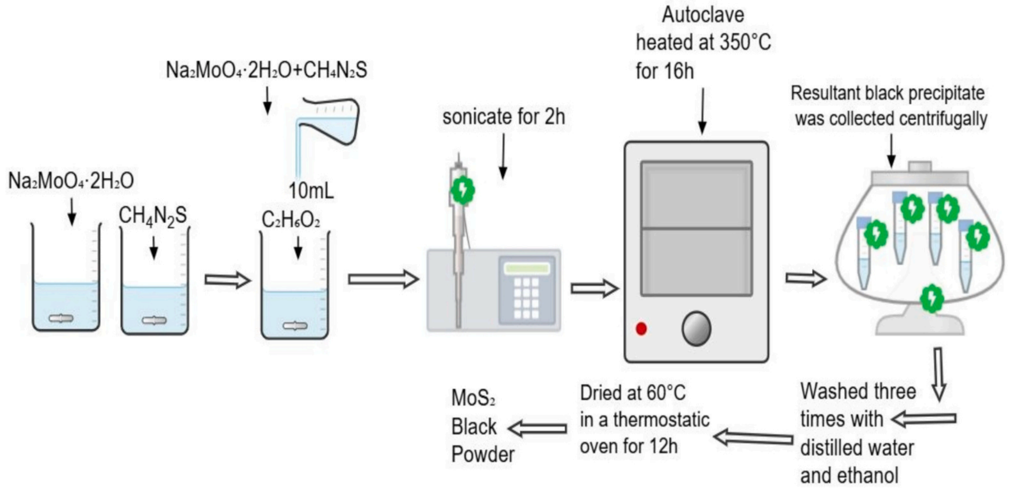

Fig. 3. Synthesis of MoS_2 nanosheets.

to the specific binding of CEA and the antibodies. This process took an hour. The final layer of the biosensor was made with the analyte Carcinoembryonic Antigen (CEA). For calibration and analysis of sensitivity at various levels, 10 μL of CEA Solution was spread on the surface of each electrode. He was then incubated at 4 °C for 1 h to promote interaction of specific antibody and antigen. Last, the biological layer was washed with a buffer solution to remove unbound CEA so that the final PEC signals are generated only from the bio specifically bound biomolecules (Fig. 4) [6].

2.3. Characterization and photoelectrochemical analysis

The synthesized materials and fabricated electrodes were systematically characterized using complementary analytical techniques to evaluate their structural, optical, morphological, and photoelectrochemical properties. UV–visible spectroscopy was employed to investigate the optical absorption behavior of the materials and assess their light-harvesting capability [19]. X-ray diffraction (XRD) analysis was used to determine the crystalline structure, phase composition, and crystallinity of the synthesized materials. Scanning electron microscopy

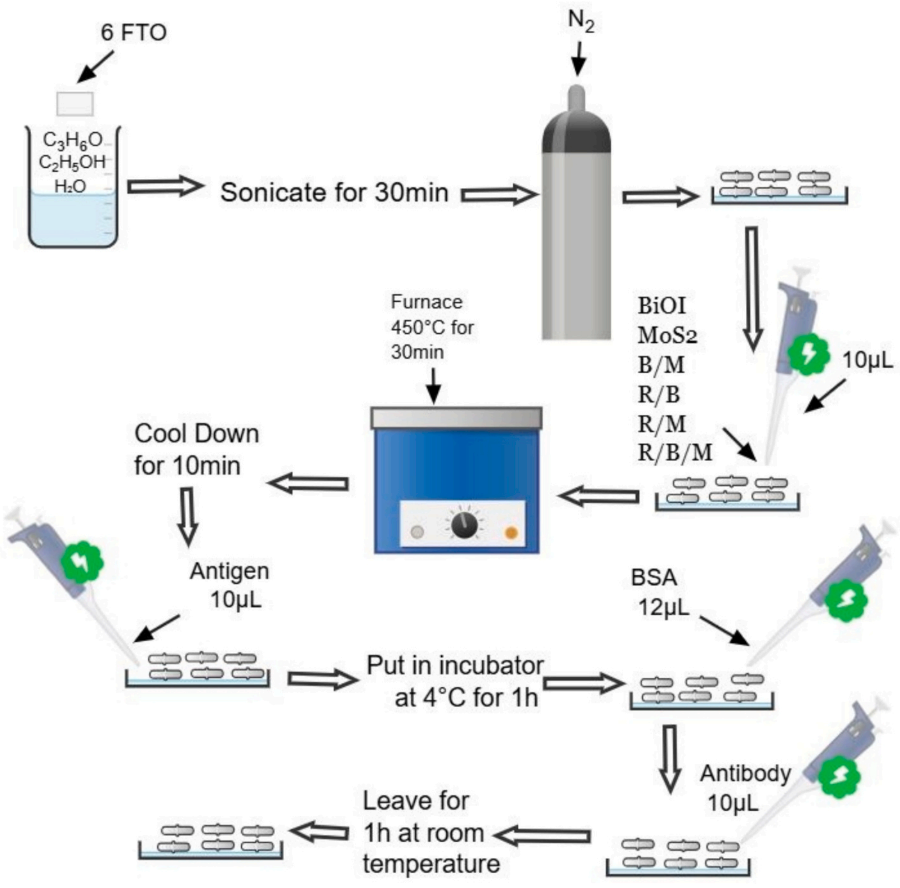

Fig. 4. PEC immunosensor fabrication process.

(SEM) was utilized to examine the surface morphology, particle distribution, and film uniformity of the synthesized materials and modified electrodes, providing insights into structural features relevant to photoelectrochemical performance [20]. Photolectrochemical properties and interfacial charge-transfer behavior were evaluated using cyclic voltammetry (CV) in a conventional three-electrode configuration, with the modified FTO electrode as the working electrode, a reference electrode (Ag/AgCl), and a platinum counter electrode. CV measurements provided information on redox behavior, electrode stability, and conductivity enhancement resulting from heterostructure formation [21]. Mott–Schottky analysis was performed to investigate the semiconductor characteristics of the photoactive materials, including carrier type, carrier density, and flat-band potential.

3. Results and discussion

3.1. UV–visible spectroscopy analysis

UV–visible spectroscopy was employed to investigate the optical absorption characteristics and electronic transitions of the synthesized materials BiOI, BiOI/MoS_2, rGO/BiOI, rGO/BiOI/MoS_2, MoS_2 and rGO/MoS_2 as light-harvesting efficiency plays a decisive role in governing photoelectrochemical (PEC) performance. The absorption spectra of BiOI, MoS_2, and their binary and ternary composites are presented in Fig. 5, while the corresponding Tauc plots used for bandgap determination are shown in Fig. 6. The extracted bandgap values are summarized in Table 1.

All synthesized materials as demonstrated in Fig. 5 possessed strong transmission in the visible-light region, thereby making them suitable for PEC applications driven by visible-light. Since they possessed relatively low bandgap energies, the materials can be electronically excited in the presence of low-energy photons. Among the components, pristine MoS_2 has an absorption spectrum that extends from the visible region to the near-infrared region. The few-layer MoS_2 that is two-dimensional (in its structure) is characterized by such an optical response, and its thickness draws quantum confinement effects. Consequently, the optical absorption of MoS_2 is strong and the associated band gap width is slightly more than that of the bulk MoS_2. As a result, the bandgap is approximately 1.92 eV and the absorption edge of MoS_2 is near 550 nm. Coupling MoS_2 and rGO, the absorption edge is red shifted to around 600 nm. The bandgap is now 1.83 eV, and the observed bandgap narrowing is due to intense interfacial electronic bonding of MoS_2 and rGO, which is less than the bandgap of the individual materials. This can be attributed to the electronic coupling between the π-states of rGO and the band-edge states of MoS_2 that can modify the band structure and introduce new energy levels near the band edges. Partial delocalization of charge carriers into the rGO network reduces quantum confinement effects [22].

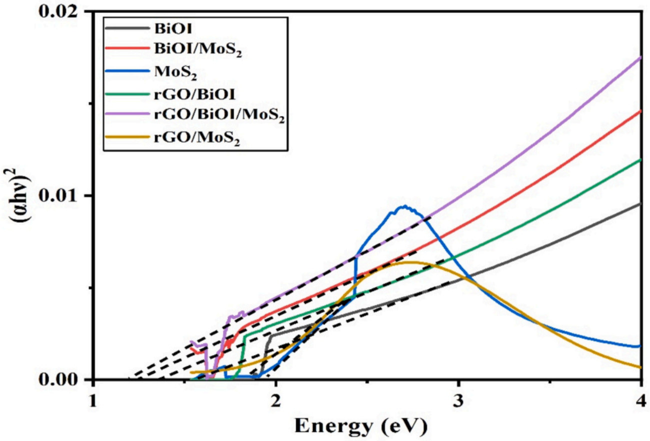

Fig. 6. Band gap spectra of BiOI, BiOI/MoS_2, rGO/BiOI, rGO/BiOI/MoS_2,MoS_2 and rGO/MoS_2.

Table 1
Calculation of band gap from Tauc plot.

Materials	Absorbance edge (nm)	Band gap (eV)
MoS_2	550	1.92
rGO/MoS_2	600	1.83
BiOI	660	1.59
rGO/BiOI	741	1.38
BiOI/MoS_2	764	1.25
rGO/BiOI/MoS_2	769	1.19

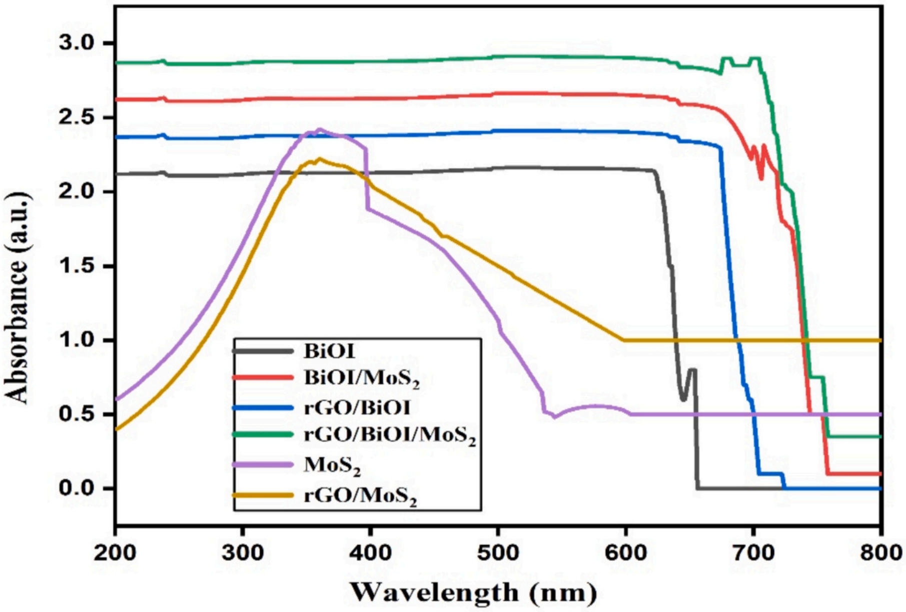

Fig. 5. The UV–Vis spectra of BiOI, BiOI/MoS_2, rGO/BiOI, rGO/BiOI/MoS_2, MoS_2 and rGO/MoS_2.

BiOI has an absorption edge of about 660 nm and an associated bandgap of 1.59 eV. The absorption behavior of BiOI derives from its unique layered crystal structure and from the Bi 6 s and O 2p orbital hybridization due to which efficient visible light excitation is possible. The edge absorption of BiOI shifted to longer wavelengths (about 741 nm) and the bandgap reduced to 1.38 eV due to the coupling of BiOI with rGO (Table 1). This is due to rGO role as a charge carrier and recombination acceptor which decreased recombination of charge carriers and lowered the excitation threshold. The most distinct changes in the optical behavior of heterostructure BiOI/MoS_2 and rGO/BiOI/MoS_2 has been noted. These heterostructure have been reported to have absorption with edges in the near-infrared region measured at about 764 and 769 nm, respectively, and to exhibit most improved optical behavior. Their bandgap energy was determined at 1.25 and 1.19 eV respectively. The pronounced bandgap narrowing is due to the synergistic effects in the microstructure of the composites to have a closer interfacial contact zone between the BiOI and the MoS_2 which is favorable to charge transfer and band overlap. The rapid electron-transport pathways and reduction of charge recombination losses from having rGO in the heterostructure increased the synergistic effects noted [23]. The Tauc method allows for a more quantitative estimate of the bandgap values that are shown in Fig. 6, calculated by extrapolating the linear portions of the plots of $(\alpha h\nu)^2$ vs. photon energy to the energy axis. The composite system's Tauc plots systematically shifted to lower energies, confirming the bandgap is narrowing further upon the formation of the heterostructure. This indicated that the composite materials require less photon energy to generate charge carriers, which is beneficial for PEC applications [24].

The overall combined assessment indicated that MoS_2 heterostructure engineering markedly improved visible-light absorption and reduction of bandgap energies. These optical enhancements solidify the potential for increased charge-carrier generation and efficient charge separation [25]. This likely accounts for the extraordinary photoelectrochemical performance of the systems, as evidenced in the subsequent electrochemical and PEC studies of BiOI/MoS_2 and rGO/BiOI/MoS_2.

3.2. X-ray diffraction (XRD) analysis

X-ray diffraction (XRD) analysis was carried out to elucidate the crystalline structure, phase composition, and structural integrity of the synthesized BiOI, MoS_2, and BiOI/MoS_2 heterostructure, as crystallinity and phase purity plays a critical role in charge transport, recombination dynamics, and interfacial charge separation in photoelectrochemical systems [26]. The XRD patterns of pure MoS_2, pure BiOI, and the BiOI/MoS_2 composite are presented in Fig. 7.

BiOI diffraction pattern in Fig. 7 showed well-defined peaks at 20.5°, 30.5°, 32.5°, 41.1°, 45.6°, and 56.6°, matching the (0 0 2), (1 0 2), (1 1 0), (0 0 4), (1 0 4), and (2 1 2) planes of tetragonal BiOI (JCPDS No. 10-0445), confirming phase purity. These peaks also reflect high intensities and a dominant (1 0 2) and (1 1 0) peak suggesting a higher degree of crystallinity, confirming the (1 0 2) and (1 1 0) planes as preferential growth directions, consistent with the layered BiOI structure. The overall anisotropic growth behavior of BiOI is most pronounced along the (1 0 2) and (1 1 0) directions, which supports the PEC devices for charge carrier transport.

The XRD pattern of pure MoS_2 in Fig. 7 showed peaks around 32.2°, 40.7°, 47.4°, and 59.8° which are attributed to the MoS_2 hexagonal structure with the (1 0 0), (1 0 3), (1 0 5), and (1 1 0) planes (JCPDS No. 37-1492). MoS_2 peaks are less intense and broader than BiOI peaks. The low peak intensity and enormous range is typical for few-layer 2D MoS_2 nanosheets. An evident sense of low crystallinity is typical for this synthesis method, and it is not a negative thing. It can instead show a lot of edges, imperfections in the lattice and surface defects which are beneficial for charge transfer and for the attachment of molecules. These attributes are especially useful for PEC signal which is typically what determines the performance of a sensor.

The diffraction peaks of BiOI/MoS_2 composite in Fig. 7 are related to the individual constituent elements BiOI and MoS_2, along with the absence of additional peaks related to impure phases, confirms the construction of heterostructure without modification of the fundamental crystalline structure of individual elements. The presence of distinct metric peaks from the two phases indicated that MoS_2 is well incorporated into the BiOI matrix rather than undergoing a structural collapse. The gradual increase of the (002) peaks from MoS_2 indicated a better dispersion and stronger contact between the MoS_2 nanosheets and the BiOI nanoparticles. The XRD analysis confirmed the successful formation of the BiOI/MoS_2 heterostructure while preserving the distinct crystalline phases of both components. The absence of significant peak shifts or additional impurity peaks indicated that no undesired phase transformation or structural collapse occurred during heterostructure formation. This suggests that the interaction between BiOI and MoS_2 primarily involves interfacial electronic coupling rather than lattice distortion. The coexistence of well-defined diffraction peaks

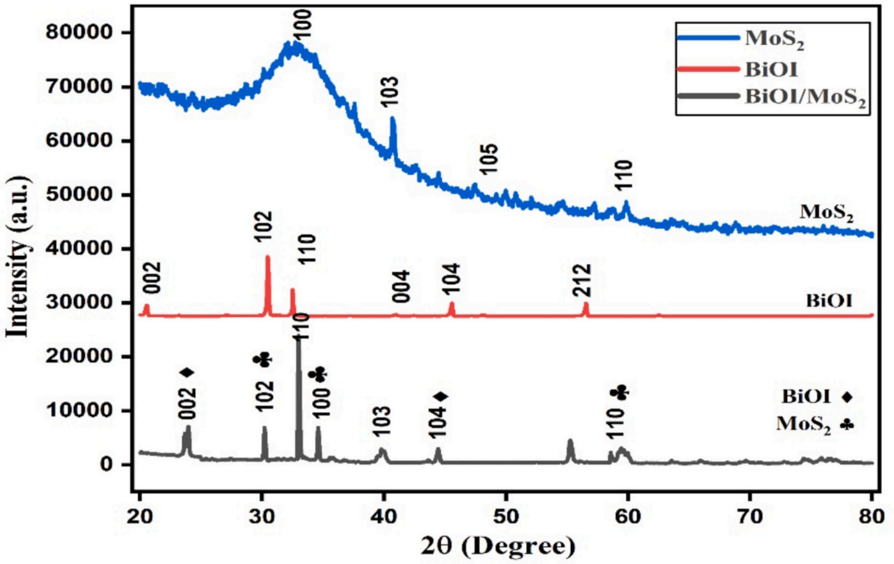

Fig. 7. XRD patterns of MoS_2 and BiOI and BiOI/MoS_2 nanocomposite.

corresponding to each material demonstrated the structural integrity of the heterojunction, which is essential for efficient charge transfer. Such a stable and crystalline heterostructure facilitated effective separation of photogenerated electrons and holes at the interface, thereby reducing recombination losses, as supported on PEC analysis below. Consequently, the XRD results provided strong evidence supporting the enhanced photocurrent response, improved charge transfer kinetics, and superior photoelectrochemical sensing performance discussed in the following sections.

3.3. *Morphological analysis by SEM*

The surface microstructure of the synthesized MoS_2, BiOI, and rGO/BiOI/MoS_2 composite was analyzed with a scanning electron microscope (SEM). As morphology is fundamental for the surface area, interfacial contact, charge-transfer kinetics, and biomolecule immobilization in photoelectrochemical (PEC) systems, the SEM images shown in Fig. 8 were analyzed to determine the microstructure of the composites formed.

The SEM image of MoS_2 Nano sheets (Fig. 8a) showed a well-structured two-dimensional morphology of thin and overlapping nanosheets that are randomly oriented, exhibiting smooth basal planes and sharp and exposed edges. This sheet-like structure is typical for layered MoS_2 and is due to the S–Mo–S sandwich structure and the anisotropic crystal growth of the sheets. Because the nanosheets are loosely stacked and are wrinkled, the effective surface area is significantly increased along with the exposure of a fair amount of active sites, that are generally more electrochemically active than the basal planes. These edge enriched features possessed a great number of active sites and charge transfer while also providing adequate sites for anchoring the antibodies. In addition, the charge diffusion pathways are shortened due to the nanosheet thin structure, thus recombination losses are reduced and PEC efficiency is enhanced. In comparison, the SEM image of BiOI (Fig. 8b) displayed nanoparticles that are spherical and showed a more densely packed formation, and has a more uneven surface texture. Granular surface morphology is typical for solvothermally synthesized BiOI, and corresponds to the layered structures of its tetragonal crystal formation. Sphericity enhanced mechanical stability and acted as a

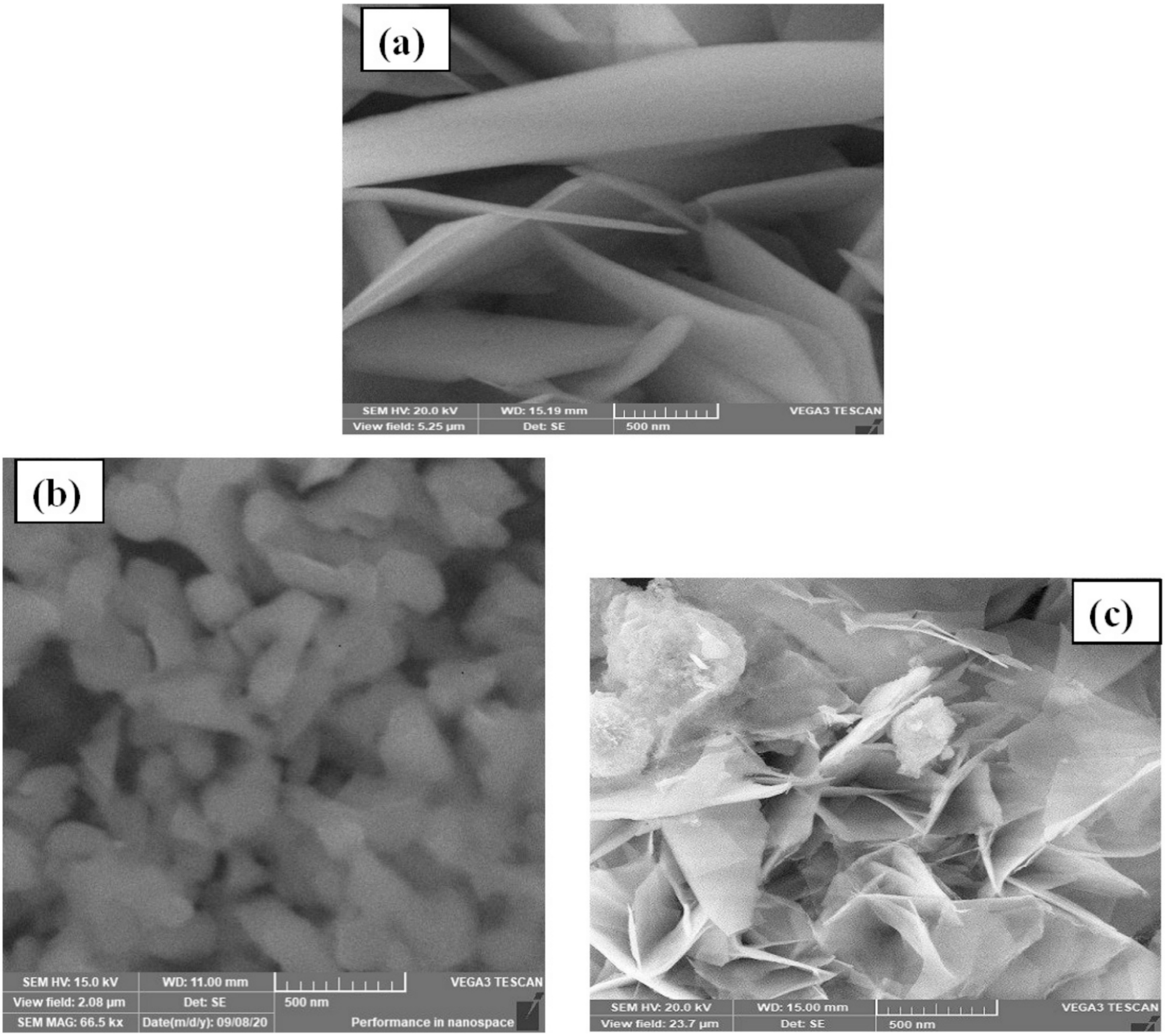

Fig. 8. SEM of MoS_2 nanosheets, (b) BiOI spherical nanoparticles, (c) rGO immunosensor response cyclic voltammetry (CV) analysis.

decent scaffolding for light harvesting. The rough texture features promoted surface contact and enhanced the anchoring of additional secondary nanoscale structures like MoS_2. The BiOI is densely packed and may constrain the movement of charge carriers. Thus, the moderate PEC performance of BiOI electrodes is explained by this factor.

The rGO/BiOI/MoS_2 composition showed a complex structure in the SEM image provided in Fig. 8c with rGO and MoS_2 nanosheets along with BiOI nanoparticles uniformly distributed, bridging the entire rGO framework. BiOI nanoparticles, and MoS_2 nanosheets are linked with thin, crumpled layers of rGO which acted as a crumpled conductive scaffold. The architecture of the rGO framework structure is the result of the strong interfacial interactions with the other semi conductive materials. The rGO framework greatly enhanced the properties of the other semi conductive components by bridging the MoS_2 and BiOI through facilitating charge transfer, reducing charge recombination, and increased enhanced light absorption. Overall, the combination of three components showed superior structural and electroactive properties. The morphological analysis stayed consistent with electroactive properties improving the PEC immunosensor response.

In order to understand the photoelectrochemical response due to the immobilization of antigen–antibody (Ab/Ag) pairs, the electrodes were subjected to cyclic voltammetry (CV) analysis through the interfacial charge transfer, a process that is fundamental to the construction of the immunosensor. CV was performed in a potassium hexacyanoferrate (III) $K_3[Fe(CN)_6]$ 1 M electrolyte solution with a potential scan between −1.0 and 1.5 V at a scan rate of 100 mV s^{-1}. The resultant CVs recorded for electrodes BiOI, MoS_2 and their binary/ternary composites, BiOI/MoS_2, rGO/BiOI, rGO/MoS_2 and rGO/BiOI/MoS_2 in the absence and presence of antigen–antibody complexes (Ag/Ab) are illustrated in Fig. 9(a–f). Here, it is noted that the symbol 'Ag' represents the carcinoembryonic antigen (CEA) which was covalently immobilized, and the symbol 'Ab' represents the antibody anti-CEA. After the immobilization of Ag/Ab, a decrease in the anodic peak current was recorded for all the electrodes. This indicated that a signal-off phenomenon has occurred in PEC immunosensing which, in turn, is a result of a biological screening layer that is deposited on top of the electrode. The antigen–antibody complex that was covalently immobilized to the surface of the electrode hindered the transfer of electrons between the electrode and the electrolyte by covering the active sites that are involved in electrochemistry and raising the interfacial resistance. The degree of current reduction is largely a function of the photoactive material's interfacial effectiveness, surface area, and electrical conductivity.

In the case of the BiOI modified electrode (Fig. 9a), the anodic peak from the bare electrode has a current of 12.4 mA and after Ag/Ab immobilization the current dropped to 6.8 mA. This current suppression, while modest, reflected the limited intrinsic conductivity of BiOI. BiOI has a pretty good light harvesting ability, but because of the poor charge transport properties, the current modulation because of surface blocking is small. In the case of the MoS_2 modified electrode (Fig. 9b), the anodic current dropped from 14.6 mA to 6.6 mA. This greater drop can be explained due to the 2D layered structure of MoS_2 because it had increased surface area, more edges, and better charge transport. These attributes magnified the effect of the binding of the antibody and antigen on interfacial charge transfer making it more BiOI sensitive. The greatest current suppression is for the case of the BiOI/MoS_2 heterostructure (Fig. 9c) in comparison to BiOI and MoS_2. The anodic peak current dropped from 15.8 mA to 5.4 mA. The reason for the greater modulation is due to the synergistic charge separation at the BiOI /MoS_2 heterojunction. The internal electric field at the hetero interface evened out the charge carrier separation under light giving the electrode a greater response to the surface blocking effects that are induced by the binding of the biomolecules. Consequently, the composite BiOI/MoS_2 showed greater PEC sensitivity in comparison to BiOI and MoS_2 individually.

More enhanced photoelectrochemical response was achieved with the incorporation of reduced graphene oxide (rGO). The rGO/BiOI-modified electrode (Fig. 9d) showed a notable change in anodic peak current of 17.1 mA (bare electrode) to 4.6 mA after Ag/Ab immobilization, which correlated to a roughly 3.7-fold current suppression. This improvement in modulation is due to the rGO, which is a highly conductive material. rGO facilitated efficient electron transport and minimized the recombination of charge carriers. Consequently, the interfacial charge-transfer process is highly sensitive to surface blocking due to the formation of antigen–antibody complexes. The behavior of rGO/MoS_2 nanocomposite is mostly similar but more notable. In Fig. 9e, we can see that the anodic current decreased from 19.8 mA to 4.3 mA after the binding of Ag/Ab, which provided a larger current modulation proved the synergistic effect of the electrically conductive rGO and the superior surface activity of MoS_2. MoS_2 nanosheets offered a lot of active surface sites due to their nanostructure, and separated the biomolecules and the charges efficiently. In combination with the rapid electron extraction due to the presence of rGO, we can expect a higher sensitivity to the binding of CEA. For the rGO/MoS_2/BiOI ternary heterostructure in Fig. 9f, we can observe the highest electrochemical activity. The bare electrode had a high anodic current of about 25.6 mA which proved that there is high conductivity and efficient charge transfer due to the combination of MoS_2 charge separation, rGO electron transportation, and BiOI light absorption. After Ag/Ab immobilization, the anodic current decreased to about 4.0 mA which is the greatest current suppression compared to the other electrodes. This significant decrease proved that there is a dense biological layer forming at the surface of the electrodes and that the ternary heterostructure has great sensitivity toward CEA detection [27].

The comparative anodic peak currents listed in Table 2 clearly demonstrated a systematic increase in current modulation following the sequence:

$$\mathrm{BiOI} < \mathrm{MoS_2} < \mathrm{BiOI/MoS_2} < \mathrm{rGO/BiOI} < \mathrm{rGO/MoS_2} < \mathrm{rGO/MoS_2/BiOI}$$

Histogram in Fig. 10 reflected the progressive enhancement in conductivity, surface area, and interfacial charge-transfer efficiency achieved through heterostructure engineering. The ternary rGO/MoS_2/BiOI system maximized these effects, leading to the strongest signal-off response and confirming its superiority as a PEC immunosensing platform for ultrasensitive CEA detection.

3.4. Mott–Schottky analysis

Analyzing and characterization of the Mott–Schottky (M–S) plots to identify the type of semiconductor, the charge carrier, and band-edge alignment of the materials is very significant in determining the interfacial charge separation and the photoelectrochemical (PEC) efficiency performance of MoS_2, BiOI, and the heterostructure. The M-S plots of MoS_2, BiOI, and MoS_2/BiOI are shown in Fig. 11 (a, b, and c) respectively. According to the analysis in Fig. 11a, MoS_2 has a negative slope which is indicative of p-type semiconductor behavior. As shown in Fig. 11b, a negative slope in the analysis of BiOI is indicative of p-type conductivity due to the presence of oxygen vacancies and acceptor states related to bismuth. The conductivity types of MoS_2 and BiOI, resulted in the formation of p-p heterojunction of BiOI/MoS_2 as shown in Fig. 11c. The less slope of the heterojunction BiOI/MoS_2 in comparison to pristine BiOI and MoS_2 revealed the presence of high concentration of charge carriers.

The VB levels were extracted from the extrapolation of the linear regions of the Mott Schottky plots as shown in Fig. 11a and b. The measured E_{VB} of MoS_2 and BiOI were calculated to be 1.81 and 1.06 eV respectively. The bandgaps of MoS_2 and BiOI were 1.92 and 1.59 eV respectively which were calculated from Tauc plots. The calculation process is shown as follows using the equation where E_{CB}, E_{VB} and E_g represent the energies of conduction band, valence band and band gap respectively.

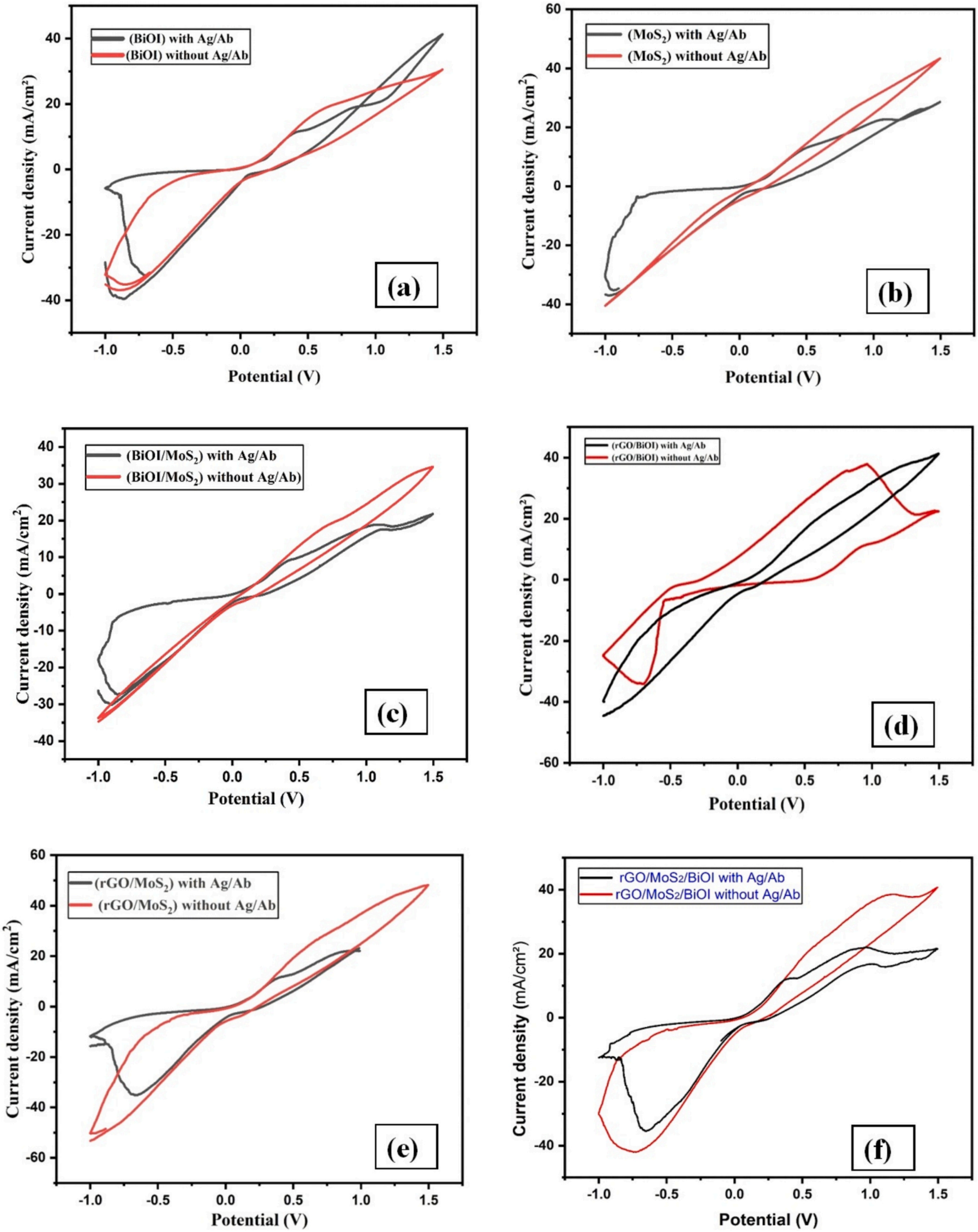

Fig. 9. Cyclic Voltammetry of (a) BiOI b) MoS_2 (c) BiOI/MoS_2 (d) rGO/BiOI, (e) rGO/MoS_2 and (f) rGO/BiOI/MoS_2.

Table 2
Anodic peak currents of the fabricated immunosensors with Ag/Ab and without Ag/Ab.

Materials	Anodic Current with Ag/Ab I_{pa} (mA/cm^2)	Anodic Current without Ag/Ab I_{pa} (mA/cm^2)
BiOI	6.8	12.4
MoS_2	6.6	14.6
BiOI/MoS_2	5.4	15.8
rGO/BiOI	4.6	17.1
rGO/MoS_2	4.3	19.8
rGO/MoS_2/BiOI	4	25.6

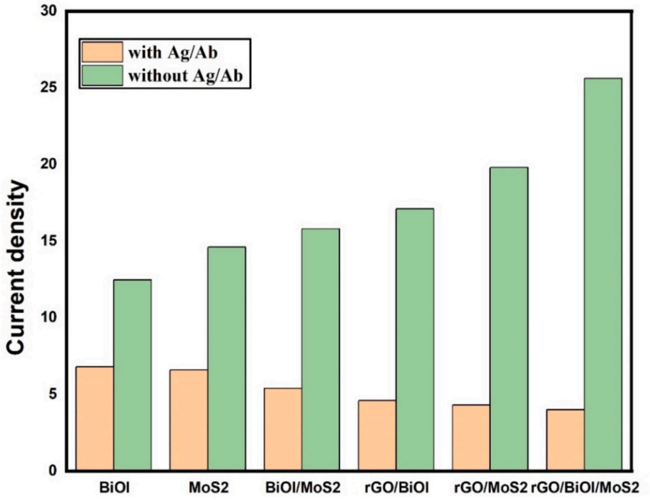

Fig. 10. Histogram of cyclic voltammetry current responses for BiOI, MoS_2, BiOI/MoS_2, rGO/BiOI, rGO/MoS_2 and rGO/BiOI/MoS_2.

$$E_{CB} = E_{VB} – Eg$$

$$E_{CB} = 1.06–1.59 = -0.53 \text{ eV}$$

$$E_{CB} = 1.81–1.92 = -0.11 \text{ eV}$$

Therefore the valence band (VB) and conduction band (CB) edge potentials for BiOI were calculated to be +1.06 eV and −0.53 eV, respectively. The VB and CB potentials for MoS_2 were calculated to be +1.81 eV and −0.11 eV, respectively. These findings suggest that BiOI has a larger negative CB potential, and MoS_2 has a more positive VB potential; thus, the two materials are well aligned for energy charge carriers transfer and distribution.

When MoS_2 and BiOI are combined, the electrons move from the higher fermi level of BiOI to lower fermi level of MoS_2 for fermi level equilibration and this transfer of charge carriers created an internal electric field (IEF) that is directed from BiOI to MoS_2 as shown in Fig. 15. This internal electric field is beneficial in that it causes oppositional movement of photogenerated charge carriers, therefore reducing the likelihood of recombination of electrons and holes. MoS_2 and BiOI when illuminated, have photogenerated electrons and holes and IEF helped these electrons to travel through the conduction band of MoS_2 to the valence band of BiOI through z scheme mechanism as IEF will not allow the transfer of electrons from BiOI to MoS_2 as shown in Fig. 15. This transfer of charge carriers created two different sites for charge collection by reducing carrier recombination. Holes in the valence band of MoS_2 will take part in oxidation of electrolyte and electrons in conduction band of BiOI will be transferred to the counter electrode. The spatial separation of charge carriers increased the lifetimes of the charge carriers and the efficiency of interfacial charge transfer. The Mott-Schottky analysis with improved band alignment and charge carrier separation matched the enhanced photoelectrochemical (PEC) response seen in the cyclic voltammetry and photocurrent measurements.

The equations below describe the process of charge generation and transfer in a photoactive heterostructure under visible light. When light is absorbed by the BiOI/MoS_2 heterostructure, it generates electron–hole pairs.

$$\text{BiOI/MoS}_2 + h\upsilon \rightarrow e^- + h^+$$

The holes participated in oxidation at the photoanode, while the electrons are transferred to the counter electrode, where they reduced ferricyanide, generating photocurrent.

$$\left[\text{Fe(CN)}_6\right]^{4-} + h^+ \rightarrow \left[\text{Fe(CN)}_6\right]^{3-}$$

$$\left[\text{Fe(CN)}_6\right]^{3-} + e^- \rightarrow \left[\text{Fe(CN)}_6\right]^{4-}$$

The *Z*-scheme mechanism is involved, with strong oxidative holes in the valence band (VB) of MoS_2 and high-energy electrons in the conduction band (CB) of BiOI. These charge carriers drived the oxidation and reduction reactions, and recombination occurs when the electron and hole meet.

$$e^-{}_{CB(BiOI)} + h^+{}_{VB(MoS2)} \rightarrow \text{recombination}$$

These M–S results showed that the developing a MoS_2/BiOI heterojunction greatly enhanced the photoelectrochemical performance of the heterostructure system in sensitive CEA detection by greatly enhancing charge separation and transport dynamics.

3.5. *Characterization of immunosensor*

Electrochemical impedance spectroscopy (EIS), was performed to evaluate the electron transfer resistance of modified electrodes of MoS_2/BiOI and rGO/MoS_2/BiOI before and after immobilizations of CEA antigen and antibodies as shown in Fig. 12. The Semicircle diameter represents the electron transfer resistance (Ret) which supports the restricted diffusion of the redox to reach the layers. The measurements were carried out in 1.0 mmol/L [Fe(CN)6]$^{3-/4-}$ solution containing 0.1 mol/L KCl. Fig. 12(a) showed that rGO/BiOI/MoS_2 coated FTO electrode have the smallest semicircle diameter providing a low electron transfer resistance. After coating of CEA antigen (curve f), semicircle diameter increased because the semiconductors and rGO combinedly reduced the ability of the redox species to access the electrode. The further immobilization of CEA antibody further increased the electron transfer resistance as shown in (c) due to insulating properties of protein. The same trend of increasing resistance was observed for the MoS_2/BiOI electrode: the lowest resistance was recorded before CEA modification (curve d), which increased after CEA antigen coating (curve b) and further increased following CEA antibody immobilization (curve e).

The fabricated immunosensors based on rGO/MoS_2/BiOI and MoS_2/BiOI coated electrodes were also characterized by PEC measurements, as shown in Fig. 13. The maximum photocurrent response was observed for rGO/MoS_2/BiOI composite as shown in curve 13a, suggesting the enhanced PEC properties of electrode, however after successive immobilization of CEA antigen and antibodies, it subsequently decreased as shown in b and c, due to the block of biomacromolecules. The similar decreasing trend of photocurrent was found to be for MoS_2/BiOI electrode as shown in Fig. 13d with more current and this current decreased successively in 13e and 13 f after immobilization of CEA antigen and antibodies.

The stability of the designed most efficient immunosensor rGO/MoS_2/BiOI was evaluated by using a prepared PEC immunosensor for 10 μg/mL CEA as shown in Fig. 14a. The photocurrent signals were detected under several on/off irradiation cycles for 220 s. Fig. 14a showed only a slight change in the photocurrent, indicating the stable developed PEC sensor for CEA detection. Fig. 14b showed the selectivity

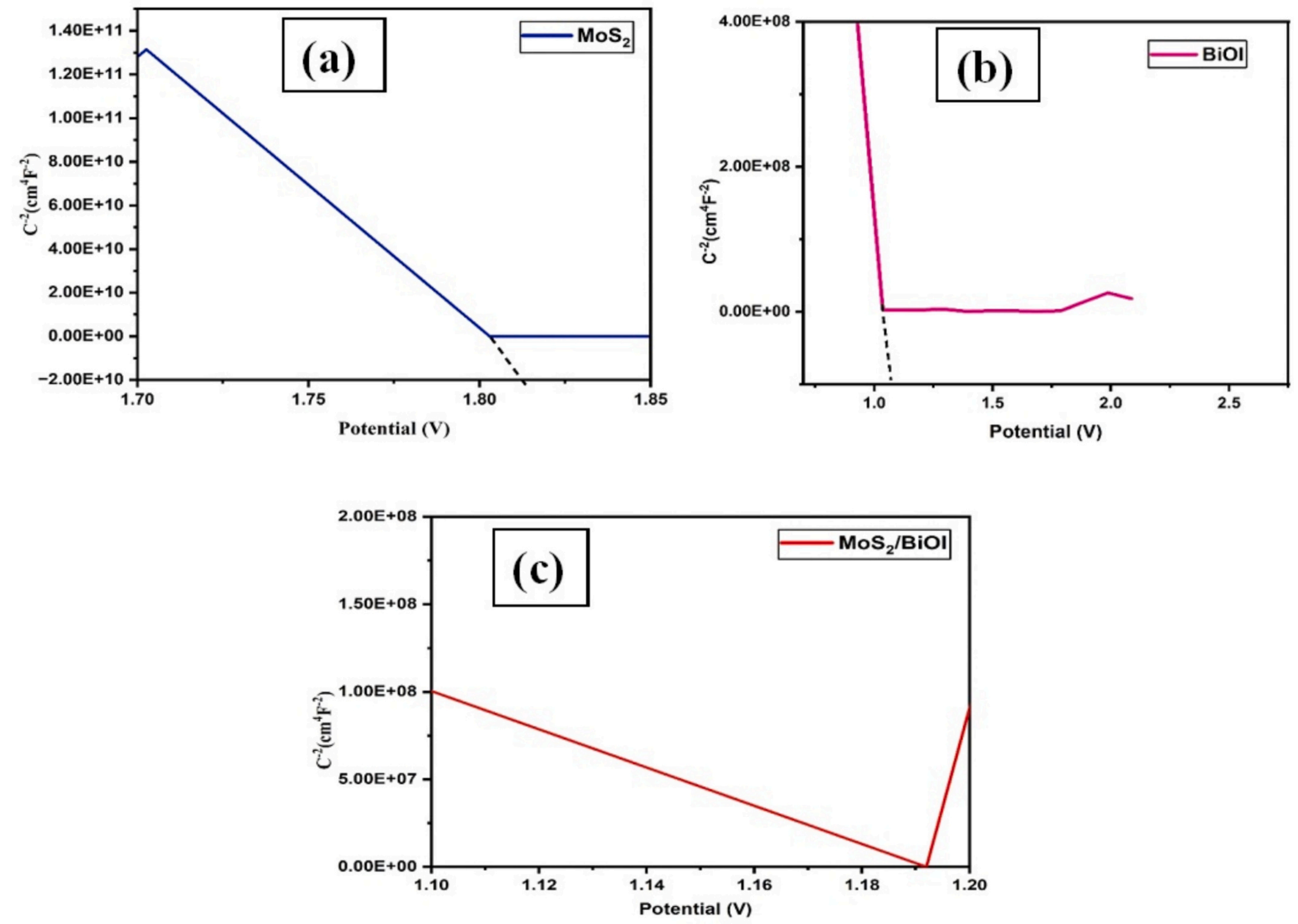

Fig. 11. The Mott–Schottky plot of a) MoS$_2$ b) BiOI, c) MoS$_2$/BiOI.

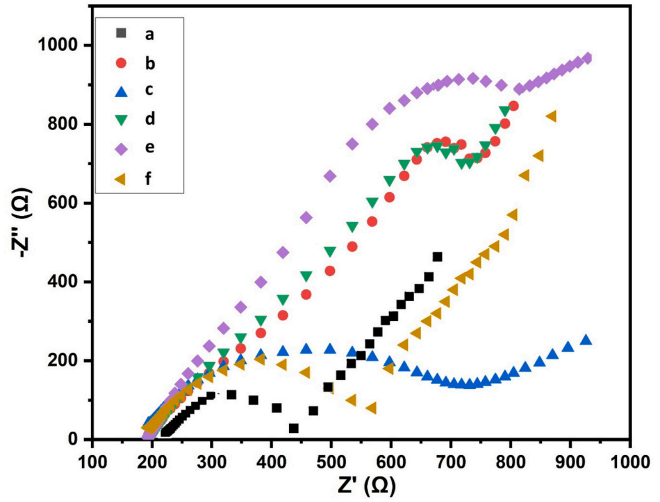

Fig. 12. Electrochemical impedance spectroscopy of (a) rGO/MoS$_2$/BiOI before CEA antigen/antibodies and (f) after antigen coating (c) after antigen/antibodies coating (d) MoS$_2$/BiOI before CEA antigen/antibodies and (b) after antigen coating (e) after antigen/antibodies coating.

of rGO/MoS$_2$/BiOI immunosensor using 10 μg/mL CEA (1), 10 μg/mL CEA + 50 μg/mL PSA (2), 10 μg/mL CEA + 50 μg/mL cholesterol (3), 10 μg/mL CEA + 50 μg/mL BSA (4), 10 μg/mL CEA + 50 μg/mL glucose (5).

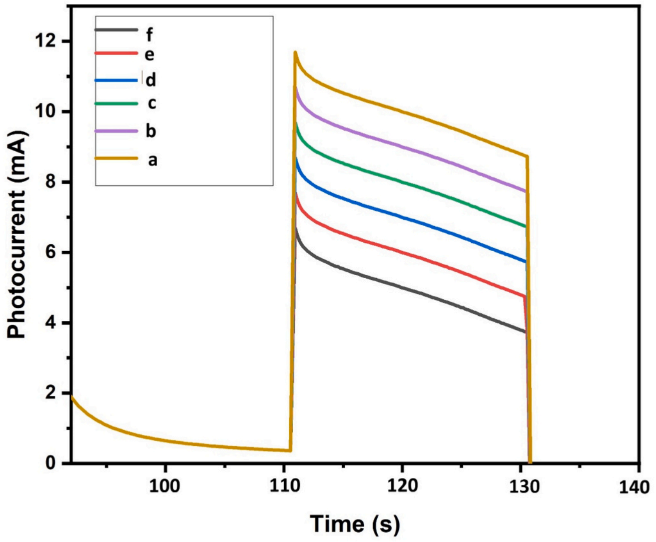

Fig. 13. Photocurrent of (a) rGO/MoS$_2$/BiOI before CEA antigen/antibodies and (b) after antigen coating (c) after antigen/antibodies coating (d) MoS$_2$/BiOI before CEA antigen/antibodies and (e) after antigen coating (f) after antigen/antibodies coating.

The photocurrent response did not change in comparison to 10 μg/mL

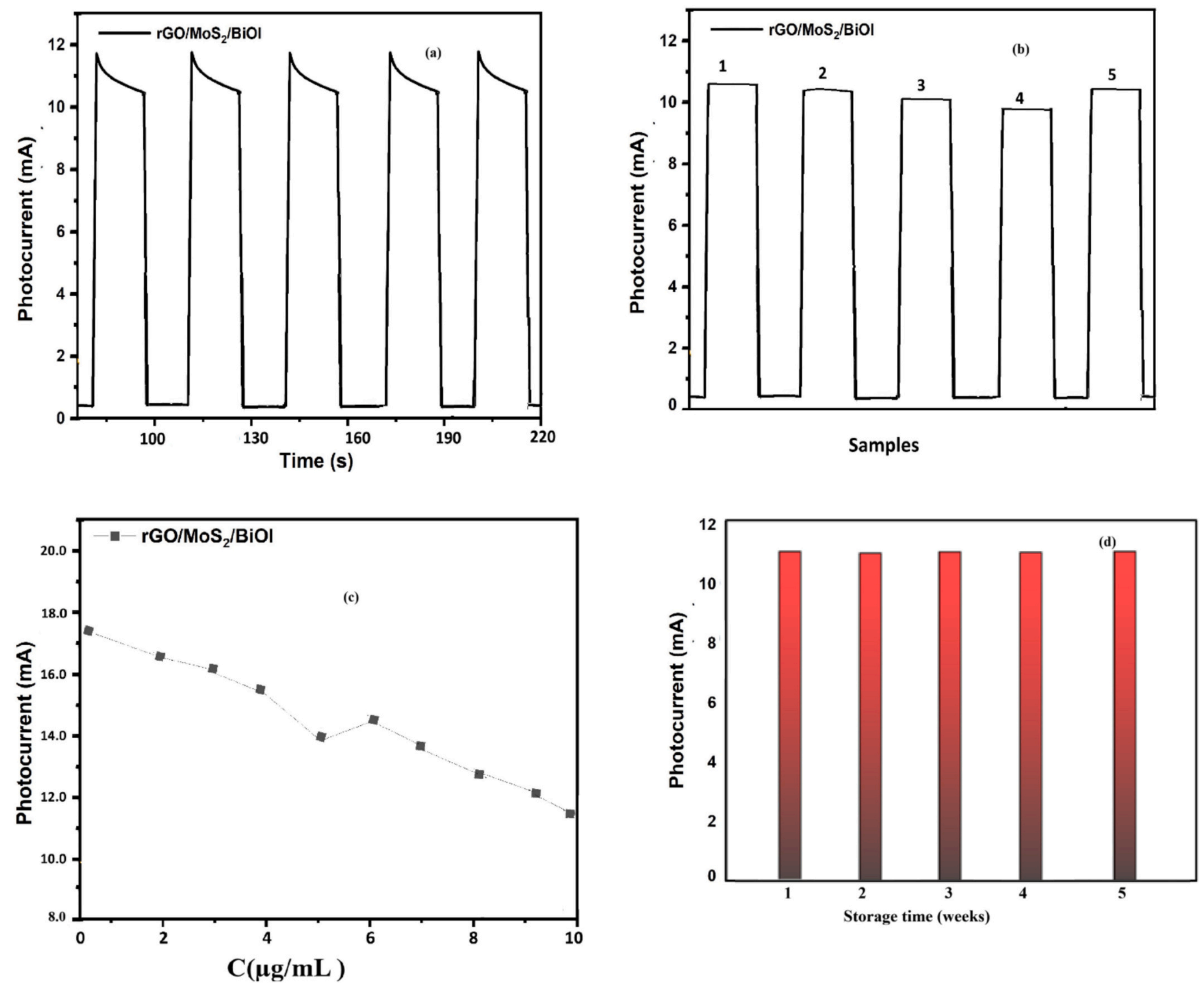

Fig. 14. (a) Stability of rGO/MoS$_2$/BiOI PEC immunosensor for 10 μg/mL CEA (b) Selectivity of the rGO/MoS$_2$/BiOI immuosensor (c) calibration curve of rGO/MoS$_2$/BiOI immunosensor for different CEA concentrations (d) reproducibility of the rGO/MoS$_2$/BiOI immunosensor.

CEA and this indicated the better selectivity of the PEC immunosensor against CEA. Different rGO/MoS$_2$/BiOI immunosensors were incubated with varying concentrations of CEA and their corresponding photocurrent were measured as shown in Fig. 14c.

The increasing concentration for CEA has decreased the photocurrents due to the insulation behavior of CEA. Fig. 14c also showed the linear decrease in photocurrent in the range from 0.01 to 10 μg/mL with a detection limit of 0.01 μg/mL indicating the good performance of PEC immunosensor. Fig. 14d revealed the same current response of the rGO/MoS$_2$/BiOI electrode for approximately 5 weeks.

3.6. Heterostructure and Z-scheme charge-transfer mechanism

PEC immunosensor BiOI/MoS$_2$ showed high PEC performance due to the mechanisms provided in Fig. 15. According to the analysis of Mott–Schottky and UV–Vis, the band alignment showed that BiOI has a VB around 1.06 eV and a CB around −0.53 eV. For MoS$_2$, the VB is around 1.81 eV and the CB is −0.11 eV. This band alignment offered the potential requisite for the effective operation of the Z-scheme. Both BiOI and MoS$_2$, under visible light, will absorb photons and as a result, will generate electron hole pairs due to the excitation of electrons from the VB to the CB. In MoS$_2$, electrons are promoted from the VB (1.81 eV) to the CB (−0.11 eV) and in BiOI, the electrons transition from the VB (1.06 eV) to the CB (−0.53 eV).

The photogenerated electrons in conduction band of MoS$_2$ preferentially recombine with the holes in the valence band of BiOI through z scheme due to the close interfacial contact and the internal electric field formed at the p-p junction. This selective recombination pathway eliminates the low-energy charge carriers that would otherwise contribute to recombination losses. Due to this scheme of recombination, high-energy electrons are kept in the conduction band of BiOI and the strong oxidative holes are left in the valence band of MoS$_2$. The electrons in BiOI conduction band will go to the counter electrode and whereas the holes in MoS$_2$ valence band will provide strong oxidation. The efficient interfacial electron transfer processes are due to the high redox potential of the separated charge carriers. This condition also leads to a reduction of the bulk recombination which greatly increased the charge carrier lifetime and, therefore, increased the photocurrent generation.

Recent studies have demonstrated that interface engineering, heterostructure design, and advanced nanomaterials significantly enhance the sensitivity and performance of photoelectrochemical and

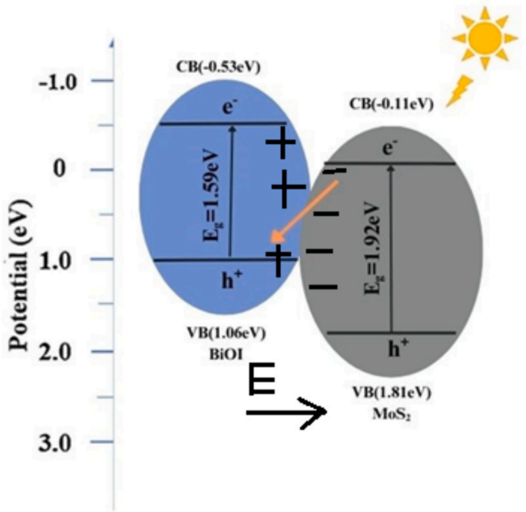

Fig. 15. Schematic diagram on photocatalytic under simulated-sunlight irradiation and charge transfer.

electrochemiluminescence biosensors. Strategies such as MOF-based systems, plasmonic nanoparticles, single-atom catalysts, and MXene-integrated composites have been widely explored for ultrasensitive detection of biomarkers, including CEA and other cancer-related analytes. These developments highlight the importance of efficient charge transfer and signal amplification in sensor design. Inspired by these advancements, the present work utilized an rGO/BiOI/MoS_2 heterostructure to achieve improved photoelectrochemical sensing performance [28–34].

Reduced graphene oxide (rGO) functioned as an efficient electron mediator by extracting the generated electrons and creating an uninterrupted conductive pathway to the FTO substrate. This electron transfer process alleviated back recombination and enhanced the photocurrent response to antigen-antibody interactions. The ternary rGO/MoS_2/BiOI heterostructure therefore provided the highest charge transfer kinetics, most intense PEC signal, and greatest sensitivity for the detection of carcinoembryonic antigen (CEA). The *Z*-scheme heterostructure not only retained charged species of a strong redox potential, but it also explained the observed improvements in optical absorption, cyclic voltammetry, Mott-Schottky, and PEC sensing [35]. These results reinforced the important function of MoS_2 as the charge-separation core and showed Z-scheme engineering can be used effectively in the development of high-performance PEC immunosensing platforms.

4. Conclusion

This research work illustrated a highly efficient photoelectronchemical sensor capable of detecting carcinoembryonic antigen via a MoS_2-based BiOI/rGO heterostructure. The designed heterostructure construction enabled the various components such as high photocatalytic activity and mitigating the individual component structures to achieve dominant component structures for high visible light charge separation and high electron transport. The construction of a p–p heterojunction of MoS_2 and BiOI and electron transfer facilitated by rGO created a robust Z-scheme charge transfer mechanism supported by optical and electrical characterization. The photoelectrochemical sensor response is due to the immuno-recognition induced blocking of the charge transfer at the sensing interface which is the detection of CEA. The ternary rGO/MoS_2/BiOI electrode received the greatest photocurrent of all the configurations which illustrates that MoS_2 played a critical role in charge transport and stimulating the system to respond. The rGO/MoS_2/BiOI PEC immunosensor demonstrated excellent stability, maintaining consistent photocurrent responses under repeated light on/off cycles. It exhibited high selectivity toward CEA, with negligible interference from coexisting biomolecules. A linear decrease in photocurrent was observed with increasing CEA concentration over the range of 0.01–10 μg/mL, achieving a low detection limit of 0.01 μg/mL. These results confirm the strong analytical performance and reliability of the developed PEC immunosensor for sensitive CEA detection. This research provided an understanding of the PEC sensing mechanisms to enhance the early diagnosis cancer bio sensing devices.

CRediT authorship contribution statement

Syeda Ammara Shabbir: Writing – review & editing, Writing – original draft, Supervision, Project administration, Investigation, Formal analysis, Conceptualization. **Amna Shahzad:** Writing – original draft, Methodology, Investigation. **Raheel Shamir Farhat:** Methodology, Investigation. **Muhammad Haris:** Writing – review & editing, Investigation. **Maryam Tahir:** Methodology, Investigation. **Safia Anjum:** Resources, Formal analysis. **Hamid Latif:** Investigation. **Carlos Ponce de Leon:** Writing – review & editing, Investigation. **Rezwan Ullah:** Formal analysis. **Tomas Tamulevičius:** Writing – review & editing, Investigation. **Sigitas Tamulevičius:** Writing – review & editing, Investigation.

Acknowledgement

This work was supported by Physics Department, Forman Christian College (A Chartered University), Lahore, Pakistan, Institute of Materials science, Kaunas institute of technology, Lithuania and Faculty of Engineering and Physics sciences, University of Southampton, UK.

Data availability

Data will be made available on request.

References

[1] M. Hariri, et al., Biosensor-based nanodiagnosis of carcinoembryonic antigen (CEA): an approach to classification and precise detection of cancer biomarker, Bionanoscience 14 (1) (2024) 429–446.
[2] S. Zhao, et al., Nanomaterial-based biosensors for carcinoembryonic antigen (CEA) detection: principles, applications, and perspectives: a review, Microchem. J. 210 (2025) 112992.
[3] T.-H. Lee, et al., Diagnostic accuracy of carcinoembryonic antigen (CEA) in detecting colorectal cancer recurrence depending on its preoperative level, J. Gastrointest. Surg. 27 (8) (2023) 1694–1701.
[4] J. Chen, et al., Smartphone-controlled portable photoelectrochemical immunosensor for point-of-care testing of carcinoembryonic antigen, Chem. Eng. J. 473 (2023) 145276.
[5] L. Zhao, C. Mao, Photoelectrochemical Immunosensor for carcinoembryonic antigen detection: an attempt for early Cancer screening, in: Advances in Fabrication and Investigation of Nanomaterials for Industrial Applications, Springer, 2024, pp. 91–109.
[6] Y. Wang, et al., Novel visible-light-driven S-doped carbon dots/BiOI nanocomposites: improved photocatalytic activity and mechanism insight, J. Mater. Sci. 52 (12) (2017) 7282–7293.
[7] K. Song, et al., Dye sensitized photoelectrochemical immunosensor for the tumor marker CEA by using a flower-like 3D architecture prepared from graphene oxide and MoS2, Microchim. Acta 185 (6) (2018) 310.
[8] D. Zheng, et al., A highly sensitive photoelectrochemical biosensor for CEA analysis based on hollow NiS@ NiO/TiO2 composite with typical pn heterostructure, Talanta 246 (2022) 123523.
[9] M. Wang, et al., A novel split-type photoelectrochemical biosensor based on liposome-induced in situ formation of Bi2S3@ BiOI/Ag2S heterojunction for the sensitive detection of CEA, Microchem. J. 200 (2024) 110388.
[10] M. Zhang, et al., Using BiOI/BiOCl composite-enhanced cathodic photocurrent and amplifying signal variation in AgI for developing a highly sensitive photoelectrochemical immunosensing platform, Chemosensors 13 (5) (2025) 164.
[11] M.M. Gul, K.S. Ahmad, Review elucidating graphene derivatives (GO/rGO) supported metal sulfides based hybrid nanocomposites for efficient photocatalytic dye degradation, Rev. Inorg. Chem. 42 (4) (2022) 337–354.
[12] X. Liu, et al., Progress in signal amplification and microstructure manufacturing for photoelectrochemical sensing, Annu. Rev. Anal. Chem. 18 (1) (2025) 383–405.
[13] A. Qureshi, T. Shaikh, J.H. Niazi, Semiconductor quantum dots in photoelectrochemical sensors from fabrication to biosensing applications, Analyst 148 (8) (2023) 1633–1652.

[14] R. Sukanya, D.C. da Silva Alves, C.B. Breslin, Recent developments in the applications of 2D transition metal dichalcogenides as electrocatalysts in the generation of hydrogen for renewable energy conversion, J. Electrochem. Soc. 169 (6) (2022) 064504.

[15] B.-Y. Shi, et al., Engineering the interface of cu/MoS2 nanostructures for improved charge transfer for applications as PEC anode materials, ACS Appl. Nano Mater. 6 (4) (2023) 2972–2984.

[16] A. Raza, et al., Photoelectrochemical energy conversion over 2D materials, Photochem 2 (2) (2022) 272–298.

[17] S. Guo, et al., Structure-controlled three-dimensional BiOI/MoS2 microspheres for boosting visible-light photocatalytic degradation of tetracycline, J. Alloys Compd. 852 (2021) 157026.

[18] X. Liu, et al., MoS2 layers decorated RGO composite prepared by a one-step high-temperature Solvothermal method as anode for Lithium-ion batteries, Nano 13 (11) (2018) 1850135.

[19] M.K. Kiteto, C.A. Mecha, Insight into the Bouguer-Beer-Lambert law: a review, Sustain. Chem. Eng. (2024) 567–587.

[20] A. Datye, A. DeLaRiva, Scanning electron microscopy (SEM), in: Springer Handbook of Advanced Catalyst Characterization, Springer, 2023, pp. 359–380.

[21] V. Periasamy, et al., Novel same-metal three electrode system for cyclic voltammetry studies, RSC Adv. 13 (9) (2023) 5744–5752.

[22] H. Li, K. Yu, C. Li, Z. Tang, B. Guo, X. Lei, Z. Zhu, Charge-transfer induced high efficient hydrogen evolution of MoS2/graphene cocatalyst, Sci. Rep. 5 (1) (2015) 18730.

[23] Y. Xu, et al., Carbon species doping overcomes the limitation of graphitic carbon nitride toward frontier photocatalysis: precise division, synergistic strategy and improvement mechanism, Adv. Energy Mater. 16 (10) (2025) e05992.

[24] M. Humayun, C. Wang, W. Luo, Recent progress in the synthesis and applications of composite photocatalysts: a critical review, Small Methods 6 (2) (2022) 2101395.

[25] K. Song, et al., Toward efficient utilization of photogenerated charge carriers in photoelectrochemical systems: engineering strategies from the atomic level to configuration, Chem. Rev. 124 (24) (2024) 13660–13680.

[26] S. Fatimah, et al., How to calculate crystallite size from x-ray diffraction (XRD) using Scherrer method, ASEAN J. Sci. Eng. 2 (1) (2022) 65–76.

[27] M. Diao, et al., A label-free photoelectrochemical immunosensor based on Sn&cd&bi ternary heterojunction: ultrasensitive detection of carcinoembryonic antigen, Microchem. J. 215 (2025) 114428.

[28] J.Z. Wu, P. Wang, A.P. Tanjung, Y. Xue, A.J. Wang, L.P. Mei, J.J. Feng, MnPP@ ZIF-8-mediated interface engineering modulation on ZnCdS/NiCoP heterojunctions: ultrasensitive photoelectrochemical aptasensor for di-2-ethylhexyl phthalate detection, Sens. Actuators B Chem. 453 (2026) 139505.

[29] L. Wu, Y. Meng, X. Zheng, Y. Bai, C. Han, Z. Wang, Y. Yao, Pillar [5] arene based prodrug as a GSH-responsive SO2 nanogenerator for effective gas cancer therapy, Chin. Chem. Lett. 36 (9) (2025) 110808.

[30] J. Wang, J. Bei, X. Guo, Y. Ding, T. Chen, B. Lu, Y. Yao, Ultrasensitive photoelectrochemical immunosensor for carcinoembryonic antigen detection based on pillar [5] arene-functionalized Au nanoparticles and hollow PANI hybrid BiOBr heterojunction, Biosens. Bioelectron. 208 (2022) 114220.

[31] Y. Wang, G. Zhao, H. Chi, S. Yang, Q. Niu, D. Wu, Q. Wei, Self-luminescent lanthanide metal–organic frameworks as signal probes in electrochemiluminescence immunoassay, J. Am. Chem. Soc. 143 (1) (2020) 504–512.

[32] G. Zhao, X. Dong, Y. Du, N. Zhang, G. Bai, D. Wu, Q. Wei, Enhancing electrochemiluminescence efficiency through introducing atomically dispersed ruthenium in nickel-based metal–organic frameworks, Anal. Chem. 94 (29) (2022) 10557–10566.

[33] F. Han, C. Cheng, J. Zhao, C. Li, Y. Wang, X. Cao, G. Zhao, Multi-element transition metal electrochemiluminescence system based on efficient quenching strategy for sensitive detection of glial fibrillary acidic protein, Sens. Actuators B 438 (2025) 137767.

[34] Y. Wang, F. Han, C. Cheng, J. Zhao, C. Li, N. Zhang, Q. Wei, Electrochemical immunosensor utilizing Zn-Fe-NC single-atom nanozyme and Ti3C2Tx@ Au for ultrasensitive detection of cytokeratins21-1, Microchem. J. 209 (2025) 112810.

[35] Wu, T., et al., Dual direct Z-scheme heterojunction with stable electron supply to a Au/PANI photocathode for ultrasensitive photoelectrochemical and electrochromic visualization detection of Ofloxacin in a microfluidic sensing platform. Anal. Chem., 2022. 95(2): p. 1627–1634.